Letter Vol. 6, No. 1 / January 2019 / Optica 15

Chiral light–matter interactions in hot vapor-cladded waveguides

Roy Zektzer, Eliran Talker, Yefim Barash, Noa Mazurski, and Uriel Levy*

Department of Applied Physics, The Benin School of Engineering and Computer Science, The Center for Nanoscience and Nanotechnology, The Hebrew University of Jerusalem, Jerusalem 91904, Israel
**Corresponding author: ulevy@mail.huji.ac.il*

Received 15 August 2018; revised 20 November 2018; accepted 1 December 2018 (Doc. ID 342492); published 21 December 2018

Recently, there has been growing interest in integrating alkali vapors with nanoscale photonic structures, such as nanowaveguides, resonators, and nanoantennas. Nanoscale confinement of electromagnetic fields may introduce a longitudinal electric field component, giving rise to circularly polarized modes that are essential for diverse applications involving vapor and light, such as chirality and nonreciprocity. Hereby, we have designed, fabricated, and characterized a miniaturized vapor cell that is integrated with optical waveguides that are designed to generate a peculiar circular-like polarization. Taking advantage of this phenomenon, we demonstrate a spectral shift in the atomic absorption signatures at varying magnetic fields, and significant isolation between forward- and backward-propagating waves in our atomic-cladded waveguide. Our results pave the way for the utilization of chip-scale integrated atomic devices in applications such as optical isolation and high spatial resolution magnetometry.

https://doi.org/10.1364/OPTICA.6.000015

Alkali vapors such as rubidium are being used in various research fields such as quantum information [1–3], nonlinear optics [4–6], magnetometry [7–9], and atomic clocks [10,11]. In the last few years, there has been a growing interest in miniaturizing rubidium cells from centimeter scale to micro- and nanoscale. On top of the obvious advantages of such integration in reducing footprint and cost, many other great qualities result from such an approach. For example, the high confinement allows one to observe significant nonlinear effects under very low optical power levels (nanowatts) [12–15]. Several miniaturized rubidium systems have been demonstrated over the last few years, e.g., the atomic-cladded waveguide (ACWG) [15,16], hollow core waveguide [17] and coupled atomic-plasmonic systems [14,18]. The combination of strong nonlinear effects and high confinement pave the way for applications such as few-photons communication systems by all-optical switching [15].

Rubidium is a highly dichroic medium due to its strong Zeeman effect, and thus has been used to realize a variety of polarization-selective and unidirectional devices such as optical isolators [19]. Basically, the Zeeman effect generates circular dichroism, i.e., two orthogonal circular polarizations are experiencing a large difference in their absorption spectrum. This effect has also been used for applications such as frequency stabilization [20], memories [2], and magnetometers [7–9]. While a rectangular waveguide supports quasi-linear polarized modes, it has been shown in systems combining waveguides and cold atoms that a strong longitudinal electric field is generated due to the strong field confinement. Thus, one can define the quantization axis by applying a magnetic field perpendicular to the propagation direction such that an atom will experience circular polarization interrogation [3]. The absorption lines of such an atom could be controlled by the strength of the magnetic field. This effect has been used for fabricating single-photon isolators [21], quantum logic gates [22], and atoms strings as Bragg reflectors [23,24]. This special polarization can also be generated by other photonic devices that confine light to the submicron scale, such as surface plasmon resonances [25] and nanoantennas. It should be mentioned that nanoantennas and metamaterials can also generate left and right circular polarizations and manipulate them by using materials with magneto-optical effect properties [26,27].

Taking advantage of the capability of generating longitudinal polarization components in a nanoscale dielectric waveguide, we have designed and fabricated an integrated nanophotonic-atomic device consisting of a photonic chip integrated with a vapor cell filled with alkali vapor. The ACWG was optimized to generate a circularly polarized light in the evanescent region. Using this chip-scale device, we have experimentally demonstrated the interaction of guided mode light with vapor in the presence of a magnetic field. In particular, we have measured the transmission spectrum through the ACWG under varying intensities of magnetic fields for input-to-output and output-to-input propagation direction and observed a strong circular dichroism. The obtained results are supported by numerical simulations.

Our hybrid ACWG-magnetic field platform is illustrated in Fig. 1. The device fabrication process begins with e-beam lithography and reactive ion etching, which defines a 3 mm long Si_3N_4 waveguide, having rib height of 0.25 μm and width of 0.6 μm, sitting on top of a thick layer of SiO_2. The device is then covered by 2 μm of SiO_2. A ~3 mm long interaction region between light and vapor is defined by the top SiO_2 using buffer hydrofluoric

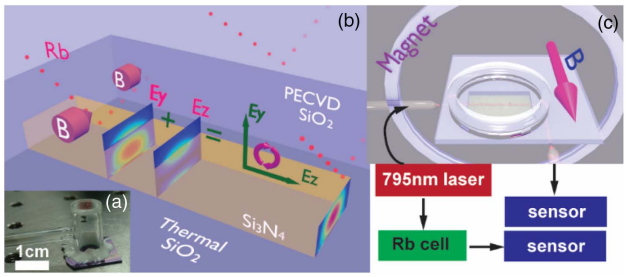

Fig. 1. (a) Device; (b) illustration of the waveguide, the optical modes, and magnetic field. The area around the waveguide, where the oxide is etched, defines the interaction region between light and vapor. (c) Schematics (not to scale) of the experimental setup.

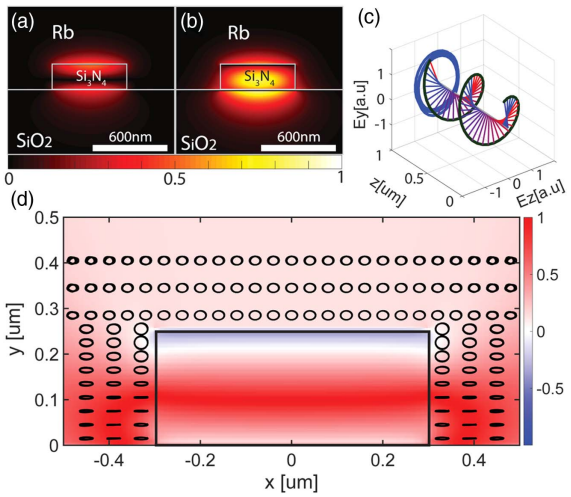

Fig. 2. (a) and (b) Magnitude of the calculated longitudinal and the transverse (vertical) electric fields. The waveguide structure is superimposed. Bright corresponds to high intensity. (c) FDTD simulation showing the evolution of polarization along the propagation axis. We have chosen a transverse coordinate located 30 nm above the top of the waveguide in the vertical direction and centered in the horizontal direction. The circular nature of polarization is evident. (d) In color, the ratio between left-handed polarization and right-handed polarization (0 corresponds to circularly polarized light). Outside of the waveguide, in the region of interaction between light and atoms, we have superimposed the polarization ellipse (as in block c). The polarization within the waveguide is not shown, as no light-vapor interactions take place within the waveguide core.

acid wet etch. A glass chamber is then epoxy-bonded to the chip. Next, the device is evacuated, filled with natural rubidium and pinched off. By doing so, a chip-scale portable device is obtained, as can be seen in Fig. 1(a). Figure 1(b) shows the schematics of the ACWG with polarization components, the TM-like mode profile and magnetic field superimposed. As can be seen, a peculiar polarization is generated owing to the existence of a strong longitudinal component of the electric field. Indeed, the polarization plane of the circularly polarized light is parallel to the light's propagation direction. In Fig. 1(c), we illustrate the experimental setup for the characterization of the fabricated device. We couple light into and out of the chip using lensed fibers and interrogate the D1 line of rubidium using a tunable laser (Toptica, 795 nm). We control the magnetic field intensity by positioning a cylinder-like magnet at different distances from the device. The magnetic field intensity and orientation are calibrated by using a Hall-effect sensor. Temperature is controlled by heating resistors that are attached to the sample. The laser detuning was calibrated by simultaneously measuring our device alongside a 7 cm long reference cell at room temperature.

First, we have numerically simulated the modes of our ACWG device. The calculated intensity profiles of the longitudinal (z) and the transverse (vertical, y) electric field modes are supported by our waveguide, as shown in Figs. 2(a) and 2(b). As we excite the TM-like mode, the electric field intensity in the x direction is an order of magnitude smaller than the field intensities along the y and z directions. Therefore, the contribution of this field component is neglected. It can be seen that in the region of the evanescent wave above the waveguide, which is the major region contributing to light-vapor interactions, the field intensities of the two field components are similar. This, combined with the $\pi/2$ phase shift between the two fields, results in an unusual circular-like polarized light. We have confirmed the existence of circular polarization by a finite-difference time-domain (FDTD) simulation and plotted the field orientation 30 nm above the waveguide [Fig. 2(c)]. We can decompose the field as $\Psi = a \cdot |E_y\rangle + b|E_z\rangle = (a-b)/\sqrt{2}|R\rangle + (a+b)/\sqrt{2}|L\rangle$. a and b are the amplitudes of the transverse ($|E_y\rangle$) and the longitudinal ($|E_z\rangle$) electric field, respectively, $|R\rangle$ and $|L\rangle$ are the right and left circular-based electric fields. The ratio between the magnitude of the electric field in the circular polarizations $(a-b)/(a+b)$ defines the purity of circular polarization, where 0 corresponds to purely circularly polarized light, 1 is transverse linear polarization, and −1 is the longitudinal linear polarization. In Fig. 2(d), we plot the ratio across the mode, with the polarization ellipse superimposed. One can clearly see that most of the region where the mode interacts with the atom the polarization is circularly polarized. In fact, by decomposing the optical mode into circular polarization basis, we have numerically found that about 93% of the optical power that resides in the evanescent tail of the optical mode is projected into one of the circular eigenstates, i.e., we have circular polarization purity of 93% in the evanescent tail of the optical mode.

Next, we simulate the effect of the application of external DC magnetic field on the D1 transitions by solving the eigenvalues of the Hamiltonian of the atom under perturbation of magnetic field [28]. We found the energy shift of each Zeeman sublevel and added a Voigt profile to each transition to account for Doppler and transit-time broadening [29]. In previous works [29], we have shown that for the case of ACWG, a larger Doppler broadening is obtained as compared to the free space due the effective refractive index of the mode being larger than unity ($n_{\text{eff}} = 1.56$), which results in Doppler broadening of about 780 MHz. Furthermore, the finite interaction time of the atom with the evanescent field results in a transit-time broadening of about 300 MHz. Combining both broadening processes results in a signal with approximately 1.1 GHz linewidth. We have added a more detailed explanation on the broadening and on finding the eigenvalues in Supplement 1. In Figs. 3(a)–3(d), we present the simulated (top panel) and measured (bottom panel) transmission spectra of our ACWG device with several values of applied magnetic field (colored lines) for left- and right-handed polarizations. The polarization can be switched either by flipping the magnet or by switching between the input and the output coupling to the device. For the data presented in Fig. 3, we have used the latter, in support of the optical isolation application. We have excited the TM-like mode

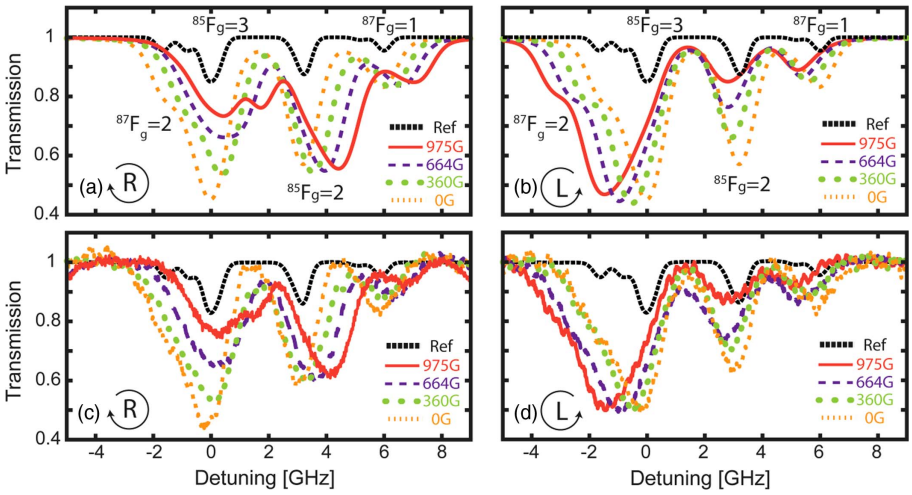

Fig. 3. (a) and (b) Simulated transmission spectra of the ACWG with different magnetic fields. (a) Right-handed; (b) left handed polarization. (c) and (d) Measured transmission spectra of the ACWG with different magnetic fields; (c) right-handed; (d) left-handed polarization. Spectroscopy data were captured at temperature of 110°. Spectroscopy data from the reference cell are captured at temperature of 25° and presented not to scale.

supported by our waveguide using polarizing-maintaining lensed fibers to ensure the launching of the circularly polarized mode. The coupling loss from the external fiber to our ACWG was measured to be ∼15 dB, from which we deduce that the power in the waveguide is ∼5 nW, an order of magnitude less than the saturation power [29]. The device was heated to 110° by using resistors; due to the small size of the device, we could heat it without heating the magnet beyond its operation temperature (80°). As a reference, we have recorded simultaneously the rubidium absorption line in a reference rubidium cell (black lines). From the result, one can notice four signatures of absorption, due to the combined transitions from the two ground levels of Rb^{85} and the two ground levels of Rb^{87}. Furthermore, one can clearly observe a significant change in the transmission spectrum as a function of the applied magnetic field. There is a distinct shift in absorption signatures. The direction of the shift is determined by the polarization. In Fig. 3, panels (a) and (c) (σ_+) one can clearly observe a blueshift of the absorption spectrum. This shift is a direct result of the Zeeman effect. For example, at 975 G, there is a ∼1.2 GHz blueshift of the absorption signature that is associated with the $F = 2$ ground level of Rb^{85}. On the other hand, in panels (b) and (d) (σ_-), we can clearly observe a redshift of the absorption spectrum. For example, at 975 G, there is a ∼1.5 GHz redshift of the absorption signature that is associated with the $F = 3$ ground level of Rb^{85}. Furthermore, we can observe both in the simulation (a) and the measurement (c) a blueshift of the absorption signatures resulting from the $F = 2$ ground level of Rb^{87} and the $F = 3$ ground level of Rb^{85}. These signatures cannot be fully resolved due to Doppler and transit-time broadening, thus resulting in a saddle pattern in their spectral response. Generally speaking, there is a good agreement between our simulation and measurement due to the high purity of circular light in the evanescent interaction region. We also observe what seems to be a contrast reduction of the other ($F = 2$ for σ_- and $F = 3$ for σ_+) absorption signature of Rb^{85}. This is due to the larger difference in Zeeman shift of the sublevels. While there is a good agreement between our simulations and measurements, there are small differences resulting mostly from facet reflections, introducing etalon effects in our devices.

In Fig. 4, we present the measured transmission of light through the device in right- and left-polarized configurations for three values of the magnetic field. To estimate the capability of the device to act as an isolator, we define an isolation ratio given as the ratio of absorption between the two orthogonal circular polarizations. As can be seen, a magnetic field of 359 G [panel (a)] does not yield much isolation. By increasing the magnetic field strength to 664 G, one obtains a higher isolation ratio of about 2.5. Finally, by increasing the magnetic field to 975 G, a very high isolation ratio of ∼10 is observed. It should be noted that, in addition to isolation ratio, another important parameter is the absolute value of isolation, where isolation in the level of few tens of decibels is typically needed. While our current device shows absorption of about 50% (3 dB), we have already shown in previous works that contrast can be greatly improved by operating at higher temperatures [29], resulting in higher atom density, and by increasing the length of the active area [15]. The current operating temperature of the device is limited due to the limited temperature operation of the glue used for bonding and of the magnets. In the future, we intend to further improve the extinction ratio by the use of anodic bonding and by using chip-scale magnets. This will allow us to operate at even higher temperatures. Furthermore, longer waveguides will be used. These changes should allow

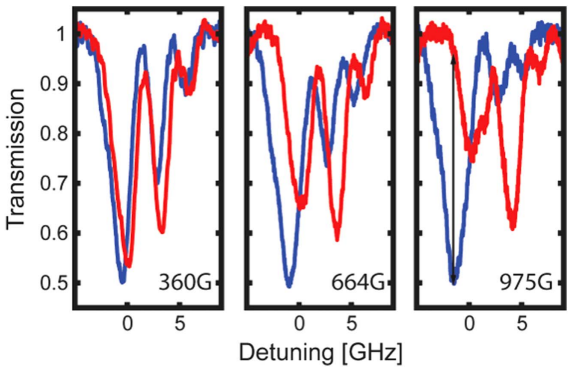

Fig. 4. Measured transmission spectra of the ACWG with different magnetic fields. Each panel compares the left- (blue) and the right-handed polarization (red). We observe optimal isolation at 975 G.

further improvement in the absolute value of isolation. With such modifications, our isolator can be implemented within communication systems operating in the few-photon regime. The enhanced broadening of the rubidium transitions in our system play a positive role, as it supports higher operation bandwidth. Another possible application for our device is in the field of magnetometry. As can be seen in Fig. 3, the device is indeed sensitive to magnetic fields. While the precision of the magnetic field sensing is expected to be somewhat limited due to linewidth broadening, the active region of detection in our device is confined to about 100 nm (the decay length of the evanescent wave), offering a tremendously high spatial resolution magnetic sensor. The high resolution makes this system a possible candidate for imaging magnetometry. While we are not yet able to achieve nanoscale resolution that can be achieved with a single nitrogen vacancy center [30] or magnetic field resolution achieved in large-scale vapor cells [8], we believe that our device provides an important step [7] toward nanoscale high-resolution magnetometry. As such, the presented approach has the potential to serve as a bridge between the above-mentioned approaches, providing both high spatial resolution and high magnetic field resolution using chip-scale technology. Future designs may also include metallic wires integrated on the chip, such that alternating magnetic fields can be applied.

In conclusion, we designed, fabricated, and experimentally characterized a chip-scale nonreciprocal ACWG device based on the integration of dielectric waveguide with alkali vapors and demonstrated the control over its transmission by the application of magnetic fields. The co-existence of a strong longitudinal field component that is in quadrature to the transverse electrical field results in a peculiar circularly polarized mode with the polarization plane parallel to the propagation direction. By the application of a magnetic field perpendicular to the polarization plane, an effective Faraday configuration is achieved, giving rise to σ^+ and σ^- transitions, depending on the polarization and the propagation direction. The experimental results, which are supported by numerical simulations, indicate isolation between the forward- and the backward-propagating beams, with a bandwidth of about 1 GHz. For a magnetic field of 975 G, very high isolation ratio is observed. Higher values of magnetic fields can be applied in the future by optimizing the geometry of the chip and the magnet. The presented platform can be a base for various applications such as isolators, high spatial resolution magnetometers, and magneto-optic modulators. This platform can also be used for the integration of many rubidium magnetic-based applications such as optical memories and frequency stabilization.

Funding. H2020 European Research Council (ERC) (ERC-LIVIN 648575); Israeli Ministry of Science, Technology and Space.

See Supplement 1 for supporting content.

REFERENCES

1. S. Rosenblum, A. Borne, and B. Dayan, Phys. Rev. A **95**, 033814 (2017).
2. M. Hosseini, B. M. Sparkes, G. Campbell, P. K. Lam, and B. C. Buchler, Nat. Commun. **2**, 174 (2011).
3. P. Lodahl, S. Mahmoodian, S. Stobbe, P. Schneeweiss, J. Volz, A. Rauschenbeutel, H. Pichler, and P. Zoller, Nature **541**, 473 (2017).
4. M. Ducloy, Phys. Rev. A **38**, 5197 (1988).
5. S. Ghosh, A. R. Bhagwat, C. K. Renshaw, S. Goh, A. L. Gaeta, and B. J. Kirby, Phys. Rev. Lett. **97**, 023603 (2006).
6. D. Budker, D. F. Kimball, S. M. Rochester, and V. V. Yashchuk, Phys. Rev. Lett. **83**, 1767 (1999).
7. P. D. D. Schwindt, S. Knappe, V. Shah, L. Hollberg, J. Kitching, L.-A. Liew, and J. Moreland, Appl. Phys. Lett. **85**, 6409 (2004).
8. I. K. Kominis, T. W. Kornack, J. C. Allred, and M. V. Romalis, Nature **422**, 596 (2003).
9. A. L. Bloom, Appl. Opt. **1**, 61 (1962).
10. P. Wolf and G. Petit, Phys. Rev. A **56**, 4405 (1997).
11. S. B. Papp, K. Beha, P. Del'Haye, F. Quinlan, H. Lee, K. J. Vahala, and S. A. Diddams, Optica **1**, 10 (2014).
12. S. M. Hendrickson, M. M. Lai, T. B. Pittman, and J. D. Franson, Phys. Rev. Lett. **105**, 173602 (2010).
13. S. M. Spillane, G. S. Pati, K. Salit, M. Hall, P. Kumar, R. G. Beausoleil, and M. S. Shahriar, Phys. Rev. Lett. **100**, 233602 (2008).
14. E. Talker, P. Arora, Y. Barash, L. Stern, and U. Levy, ACS Photon. **5**, 2609 (2018).
15. L. Stern, B. Desiatov, N. Mazurski, and U. Levy, Nat. Commun. **8**, 14461 (2017).
16. R. Ritter, N. Gruhler, W. Pernice, H. Kübler, T. Pfau, and R. Löw, Appl. Phys. Lett. **107**, 041101 (2015).
17. W. Yang, D. B. Conkey, B. Wu, D. Yin, A. R. Hawkins, and H. Schmidt, Nat. Photonics **1**, 331 (2007).
18. S. A. Aljunid, E. A. Chan, G. Adamo, M. Ducloy, D. Wilkowski, and N. I. Zheludev, Nano Lett. **16**, 3137 (2016).
19. L. Weller, K. S. Kleinbach, M. A. Zentile, S. Knappe, I. G. Hughes, and C. S. Adams, Opt. Lett. **37**, 3405 (2012).
20. V. V. Yashchuk, D. Budker, and J. R. Davis, Rev. Sci. Instrum. **71**, 341 (2000).
21. C. Sayrin, C. Junge, R. Mitsch, B. Albrecht, D. O'Shea, P. Schneeweiss, J. Volz, and A. Rauschenbeutel, Phys. Rev. X **5**, 041036 (2015).
22. I. Shomroni, S. Rosenblum, Y. Lovsky, O. Bechler, G. Guendelman, and B. Dayan, Science **345**, 903 (2014).
23. H. L. Sørensen, J.-B. Béguin, K. W. Kluge, I. Iakoupov, A. S. Sørensen, J. H. Müller, E. S. Polzik, and J. Appel, Phys. Rev. Lett. **117**, 133604 (2016).
24. N. V. Corzo, B. Gouraud, A. Chandra, A. Goban, A. S. Sheremet, D. V. Kupriyanov, and J. Laurat, Phys. Rev. Lett. **117**, 133603 (2016).
25. L. Stern, M. Grajower, N. Mazurski, and U. Levy, Nano Lett. **18**, 202 (2018).
26. I. Zubritskaya, N. Maccaferri, X. I. Ezeiza, P. Vavassori, and A. Dmitriev, Nano Lett. **18**, 302 (2018).
27. J. Bar-David, L. Stern, and U. Levy, Nano Lett. **17**, 1127 (2017).
28. P. Tremblay, A. Michaud, M. Levesque, S. Thériault, M. Breton, J. Beaubien, and N. Cyr, Phys. Rev. A **42**, 2766 (1990).
29. L. Stern, B. Desiatov, I. Goykhman, and U. Levy, Nat. Commun. **4**, 1548 (2013).
30. J. R. Maze, P. L. Stanwix, J. S. Hodges, S. Hong, J. M. Taylor, P. Cappellaro, L. Jiang, M. V. G. Dutt, E. Togan, A. S. Zibrov, A. Yacoby, R. L. Walsworth, and M. D. Lukin, Nature **455**, 644 (2008).